TiO$_2$ Nanorods and Pt Nanoparticles under a UV-LED for an NO$_2$ Gas Sensor at Room Temperature

Jinhong Noh [1], Soon-Hwan Kwon [2], Sunghoon Park [3], Kyoung-Kook Kim [2,4,*] and Yong-Jin Yoon [1,5,*]

[1] Department of Mechanical Engineering, Korea Advanced Institute of Science and Technology, Daejeon 34141, Korea; jinhongnoh@kaist.ac.kr

[2] Department of Advanced Convergence Technology, Research Institute of Advanced Convergence Technology, Korea Polytechnic University, Siheung-si 15073, Korea; canwkd21@kpu.ac.kr

[3] Department of Intelligent and Mechatronics Engineering, Sejong University, Seoul 05006, Korea; s.park@sejong.ac.kr

[4] Department of Nano & Semiconductor Engineering, Korea Polytechnic University, Siheung-si 15073, Korea

[5] School of Mechanical and Aerospace Engineering, Nanyang Technological University, Singapore 639798, Singapore

* Correspondence: kim.kk@kpu.ac.kr (K.-K.K.); yongjiny@kaist.ac.kr (Y.-J.Y.)

Abstract: Because the oxides of nitrogen (NO$_x$) cause detrimental effects on not only the environment but humans, developing a high-performance NO$_2$ gas sensor is a crucial issue for real-time monitoring. To this end, metal oxide semiconductors have been employed for sensor materials. Because in general, semiconductor-type gas sensors require a high working temperature, photoactivation has emerged as an alternative method for realizing the sensor working at room temperature. In this regard, titanium dioxide (TiO$_2$) is a promising material for its photocatalytic ability with ultraviolet (UV) photonic energy. However, TiO$_2$-based sensors inevitably encounter a problem of recombination of photogenerated electron-hole pairs, which occurs in a short time. To address this challenge, in this study, TiO$_2$ nanorods (NRs) and Pt nanoparticles (NPs) under a UV-LED were used as an NO$_2$ gas sensor to utilize the Schottky barrier formed at the TiO$_2$-Pt junction, thereby capturing the photoactivated electrons by Pt NPs. The separation between the electron-hole pairs might be further enhanced by plasmonic effects. In addition, it is reported that annealing TiO$_2$ NRs can achieve noteworthy improvements in sensing performance. Elucidation of the performance enhancement is suggested with the investigation of the X-ray diffraction patterns, which implies that the crystallinity was improved by the annealing process.

Keywords: gas sensor; room temperature; photoelectrochemical performance; plasmonic effect; electron trap; TiO$_2$ nanorods; Pt nanoparticles

1. Introduction

The oxides of nitrogen (NO$_x$), which belongs to one of the toxic gases [1,2], have drawn enormous attention from researchers who develop gas sensors over the past decades. Because NO$_x$ gases are harmful to the environment and poisonous to humans, it is required that NO$_x$ sensors have high, reliable performance for real-time monitoring [3]. In this regard, to improve sensor performance, many researchers have been utilizing semiconductor metal oxides [4]. These semiconductor-type gas sensors are widely known to have a low cost and simple completion [5]. Although various sensing types have been suggested [6–10], using semiconducting metal oxides has further potential to take advantage of the growing field of nanotechnology [11].

One of the possible enhancements made by employing nanotechnology is the improved capability to work at room temperature (RT) in combination with photonic energy. Gas sensors made of metal oxide semiconductors usually work at high temperature in the range of 200–500 °C, which is likely to cause drawbacks such as limited lifetime or

sensitivity degradation [11]. To surmount these limitations, studies on RT gas sensors have flourished in recent years [12–15]. The RT gas sensors, using metal oxide semiconductors, utilize photoactivation, which is a viable alternative to thermal activation, thereby lowering the working temperature. Because various nanostructures have been found to further improve the sensor performance at RT, RT gas sensors with nanostructures that use photonic energy have been developed in many recent studies [16–20].

Another possible improvement is further performance enhancement made by loading noble metal nanoparticles (NPs) on photoactivated metal oxide semiconductors. Titanium dioxide (TiO_2) decorated with the noble metal NPs, such as Pt [21,22], Au [23,24], Pd [25,26], or Ag [27,28], is a widely known example. The charge separation, by which the photocatalytic activity is remarkably improved, is one of the expected effects, although the exact mechanism has not been disclosed clearly [29]. TiO_2 has attracted attention as a promising material for gas sensors due to its non-toxicity, inexpensiveness, stability, and photocatalytic ability [30]. However, there is an undesirable possibility that photoactivated electrons are not allowed to reach the surface for chemical reactions because the time for the recombination of the electron-hole pairs is too short. In this regard, to extend the time for the separation between the electron-hole pair, the noble metal NPs have been utilized. The noble metal NPs on TiO_2 work as electron traps by forming the high Schottky barriers at the interface, thereby significantly improving the performance [21,22,29].

In this study, NO_2 gas sensors made of annealed TiO_2 nanorods (NRs) and Pt NPs are developed to work at RT by utilizing the photoactivation and charge separation. TiO_2 NRs are fabricated by the well-known hydrothermal method [31] which has several advantages compared to the other fabrication methods [32], and subsequently, TiO_2 NRs are annealed with the expectation that the heat treatment might cause changes in crystalline characteristics and photocatalytic properties [33]. The agglomeration of Pt using rapid thermal processing is utilized to load Pt NPs on TiO_2 NRs. The as-prepared sensor is photoexcited to detect NO_2 gas at RT by using an ultraviolet light-emitting diode (UV-LED). After setting an experimental setup, gas sensing performances are tested to investigate the effects of the annealing process. Herein, it is reported that annealing TiO_2 NRs is likely to improve the performance of the RT gas sensor significantly owing to crystallinity improvement of TiO_2 NRs by thermal treatment. Lastly in the paper, plausible photocatalytic oxidation mechanisms are proposed to explain the results of the experiments.

2. Materials and Methods

2.1. Fabrication Process

Figure 1 shows the process of fabricating TiO_2 NRs loaded by Pt NPs. A fluorine-doped tin oxide (FTO) glass (14 Ω/square) was purchased from Pilkington (Japan). The FTO-coated glass was prepared after ultrasonically cleaning with EnSolv, acetone, isopropyl alcohol, and deionized (DI) water. To prepare hydrothermal precursor solution, hydrochloric acid (M = 36.46, HCl) and titanium(IV) butoxide (97%, TBO) were purchased from Daejung (Korea) and Sigma-Aldrich, respectively. 30 mL of DI water and 30 mL of HCl were mixed and stirred for 5 min. 1 mL of TBO was dropped into the solution of DI water and HCl, and the solution was stirred for 5 min. The as-prepared solution was poured into a Teflon cup and subsequently, the cleaned substrate was placed vertically in the Teflon cup. After sealing the Teflon cup with a stainless steel autoclave, the autoclave was tightened to prevent leakage of the solution at an elevated temperature. The hydrothermal synthesis was conducted at 160 °C for 12 h. After cooling the autoclave and its contents, synthesized TiO_2 NRs were rinsed with DI water and dried with nitrogen gas. Subsequently, the TiO_2 NRs were annealed at 700 °C in ambient air. Herein, annealing time was controlled to investigate the effects of heat treatment. To form Pt NPs on the surface of the TiO_2 NRs, after sputtering Pt for 4 min by using the sputter coater (Cressington, 108 Sputter Coater), rapid thermal annealing (RTA) was carried out to Pt-sputtered TiO_2 NRs at 700 °C for 2 min in nitrogen ambiance. Because the RTA leads to the agglomeration

of Pt on TiO$_2$ NRs, Pt-NP-loaded TiO$_2$ NRs were obtained consequently. The abbreviations of the types of the samples used in this paper are listed in Table 1.
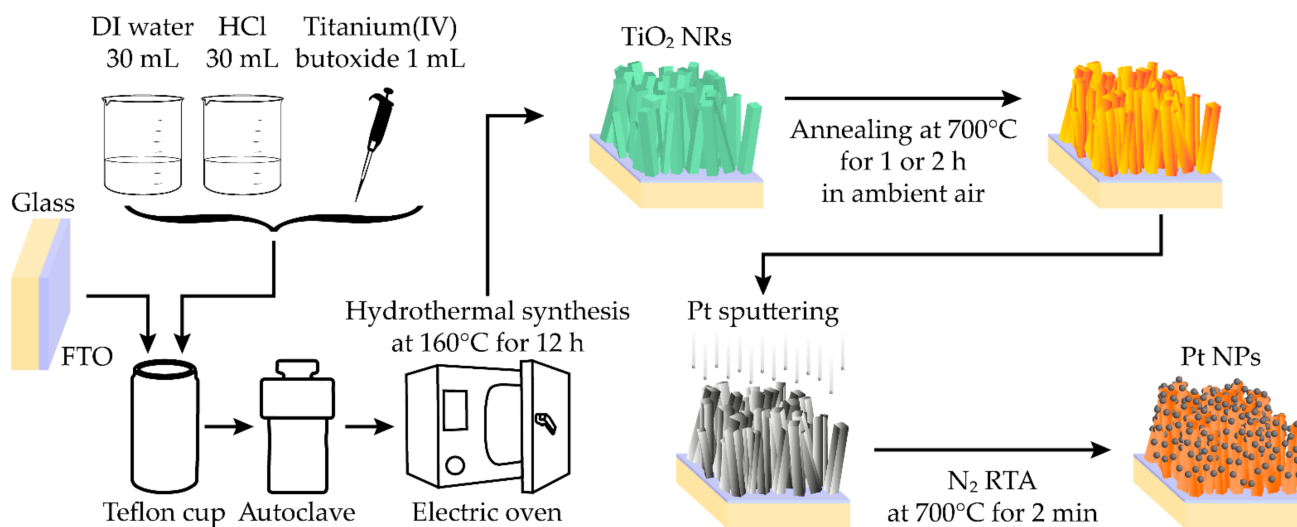
Figure 1. A schematic of the fabrication process is illustrated. The hydrothermal method is employed to obtain titanium dioxide (TiO$_2$) nanorods (NRs) on the substrate of fluorine-doped tin oxide (FTO)-coated glass. After annealing the TiO$_2$ NRs, the agglomeration of Pt is utilized by conducting rapid thermal annealing (RTA) to load Pt nanoparticles (NPs) on TiO$_2$ NRs.

Table 1. Abbreviations of the sample types are listed. The samples were fabricated by following the process illustrated in Figure 1.

Abbreviations for Sensor Types	Time for Annealing TiO$_2$ NRs at 700 °C
Sensor A	No annealing
Sensor B	1 h
Sensor C	2 h

2.2. Characterization Method

The morphologies of the prepared samples were investigated by using the field-emission scanning electron microscope (FE-SEM, FEI Company, Nova NanoSEM 200) at 10 kV. The X-ray diffraction (XRD) patterns were measured to examine the crystal phase by using the X-ray diffractometer (Rigaku Corporation, SmartLab). The measurements of XRD patterns were performed with the copper target (λ = 1.540562 Å) at 9 kW and in the range of 20° to 70° at a speed of 5°/min.

2.3. Experimental Setup for NO$_2$ Gas Sensors

Figure 2 depicts a schematic of an experimental setup where the as-prepared samples were tested for sensing NO$_2$. Dry air and NO$_2$ gas flowed into a customized controller to obtain concentrations, such as 5 ppm, 10 ppm, or 15 ppm. Mass flow controllers and air drive forming machines were deployed in the controller, and the control system was manipulated by using LabVIEW software. The 500 sccm of target gas of which concentration was controlled filled a test chamber and subsequently, flowed out through the outlet. The inset in Figure 2 shows a schematic inside the test chamber. The UV-LED of which wavelength is 370 nm was located on the top inside the chamber and driven by the power supply (MKPOWER, MK3005D, at 20 mA) which was placed outside of the chamber. The UV-LED remained on during the test experiments. The sample of the gas sensor, of which dimensions were 2 cm × 2 cm, was laid on the center of the bottom. The positions of the probes were adjusted with the stages connected through the wall of the chamber. Electrical signals from two probes were sent to the multimeter (Keithley,

2700 Multimeter). Lastly, the data of the resistance was plotted on the laptop. Every experiment was conducted at RT around 20 °C.
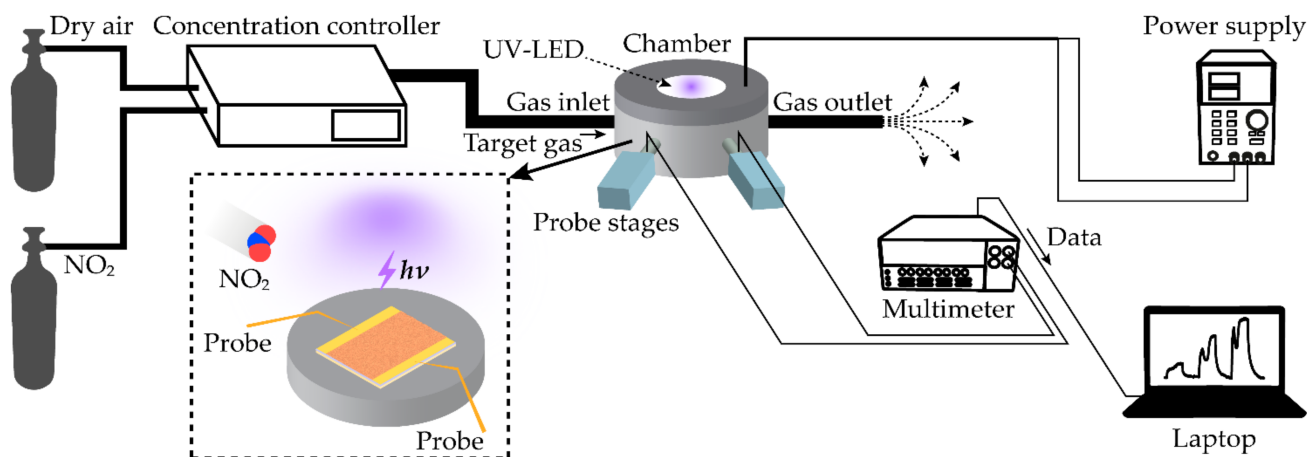
Figure 2. An experimental configuration of measuring gas sensing properties is depicted. The concentration controller is a customized system which controls concentrations of the target gas. The inset shows a schematic diagram describing the test chamber. The UV-LED is attached to the top surface. The sample of the gas sensor is laid on the bottom. On the laptop, resistances of the sample obtained by the multimeter are plotted in real-time.

3. Results and Discussion

3.1. Characterization

Figure 3 shows the morphology of the samples fabricated following the process depicted in Figure 1. It is confirmed that TiO_2 NRs were grown evenly. The average density of the number is obtained as $36/\mu m^2$ approximately by counting the NRs in the FE-SEM images of Figure 3. There are adequate sites for the target gas to be adsorbed on the surface, thereby probably increasing the gas sensing performance [22]. Figure 3a–d present the results before and after loading Pt NPs, respectively. TiO_2 NRs in Figure 3e–h were annealed for 1 h and 2 h, respectively, and decorated with Pt NPs. Namely, Figure 3c–h are the FE-SEM images of Sensor A, Sensor B, and Sensor C, respectively. Based on the FE-SEM images of Figure 3, the TiO_2 NRs have an average diameter of about 83 nm with a standard deviation of around 21 nm. Whereas the size of the Pt NPs in Figure 3c,d is around 13–42 nm, the Pt NPs in Figure 3e,h have the size of 13–18 nm approximately. In addition, as shown in Figure 3c,d, for the TiO_2 NRs which did not have an annealing process, the Pt NPs on the top surface agglomerated together to form a chunk of Pt. Lastly, cross-junctions between NRs contacting each other which offer pathways for electrons are observed [34].

The XRD patterns are shown in Figure 4 to investigate the crystallinity of the TiO_2 NRs. Figure 4a shows the XRD pattern of the substrate before synthesizing TiO_2 NRs, and the peaks are denoted by the asterisks. The XRD pattern of Sensor A is plotted in Figure 4b. In this case, TiO_2 NRs did not have an annealing process before loading Pt NPs. Compared to Figure 4a, two peaks emerge at 36.1° and 62.7° which correspond respectively to the rutile (101) and (002) peaks referred by JCPDS card no. 21-1276. Because the hydrothermal method used in this study initiates the (101) facet more easily, it can be noticed that the peak of the (101) plane is dominant [35]. Although anatase, one of the possible crystalline forms of TiO_2, is the most famous for photocatalytic activities, the rutile phase could be desirable for photocatalytic oxidation activities [36]. Figure 4c,d plot the XRD patterns of Sensor B and Sensor C, respectively. In all three cases of Figure 4b–d, the peaks of Pt do not appear. This unobservable characteristic implies that the fine Pt NPs are highly dispersed on the surfaces of TiO_2 NRs [37].
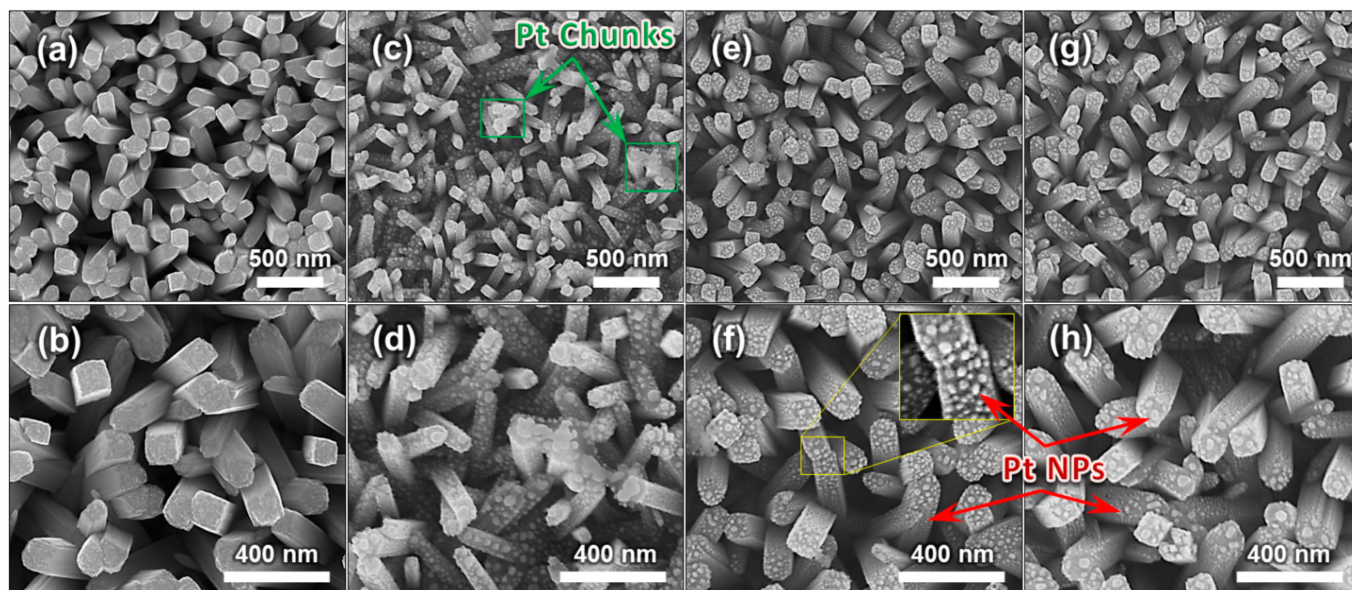
Figure 3. FE-SEM images of the gas sensors are shown. (**a**,**b**) are the results of the hydrothermal synthesis. (**c**,**d**) are TiO$_2$ NRs and Pt NPs of Sensor A. (**e**,**f**) are TiO$_2$ NRs and Pt NPs of Sensor B. (**g**,**h**) are TiO$_2$ NRs and Pt NPs of Sensor C. The inset in (**f**) shows an enlarged image to clearly display the Pt NPs on the TiO$_2$ NRs. The red arrows indicate Pt NPs. The green arrows in (**c**) indicate chunks of Pt agglomerated together on the top surface of TiO$_2$ NRs.
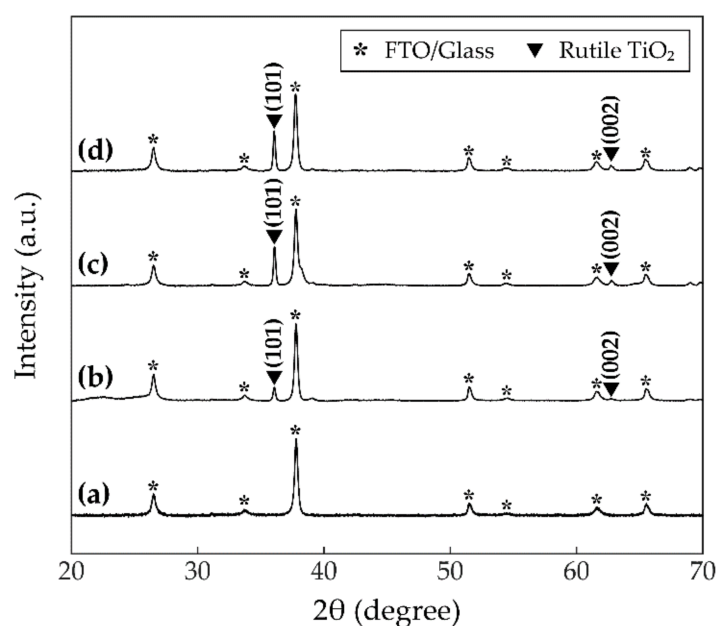
Figure 4. X-ray diffraction (XRD) patterns of (**a**) the FTO-coated glass as the substrate, (**b**) Sensor A, (**c**) Sensor B, and (**d**) Sensor C. The asterisk denotes the peak of the substrate and the triangle marker indicates the peak of the rutile TiO$_2$.

Figure 5 implies that annealing TiO$_2$ NRs in ambient air is likely to improve crystalline characteristics of the TiO$_2$ NRs [38]. The full width at half maximum (FWHM) is calculated from the XRD patterns obtained in Figure 4. Figure 5a,b show FWHMs of Figure 4b–d at rutile TiO$_2$ (101) and (002) planes, respectively, with respect to time of annealing TiO$_2$. For the (101) facet, annealing processes for 1 h and 2 h give decrements of 5.8% and 6.7% on the FWHMs relative to the FWHM of the sample without thermal treatment. Likewise, for the (002) peak, the FWHMs after annealing 1 h and 2 h are decreased by 21.7% and

31.1%, respectively. These decremental FWHMs with respect to time of annealing TiO_2 indicate incremental improvements to the crystallinity of TiO_2 NRs. It is expected to lead to enhancing electron mobility, thereby inhibiting electron-hole recombination. This suppressing recombination will offer photoactivated electrons the strong possibility to reach the surface of the TiO_2 NR, accumulate in the Pt NPs, and subsequently, provide a photoelectrochemical response.

(a)　　　　　　　　　　　　　　　　**(b)**
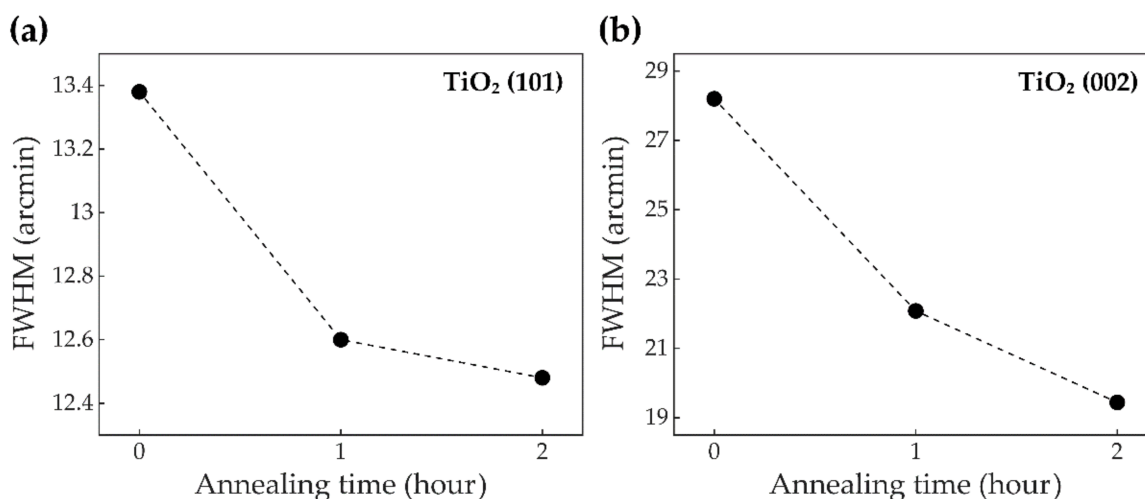
Figure 5. The full width at half maximums (FWHMs) of the XRD peaks of the rutile TiO_2 with respect to time of annealing TiO_2 are shown. (**a**) and (**b**) are the results at the (101) peaks and (002) peaks in Figure 4, respectively.

3.2. Sensor Performance

Figure 6 shows the NO_2 sensing performances at RT with the UV-LED. The experiments depicted in Figure 2 were conducted for three cases of the samples; Sensor A, Sensor B, and Sensor C. When the sensors were deployed without UV exposure, the read-outs showed only noisy signals. Figure 6a compares the results of the experiments obtained from each sample when the concentrations of the NO_2 gas were controlled to be 5 ppm, 10 ppm, and 15 ppm. For comparisons of the performance curve profiles of three sensor types, the resistance increments, relative to the value of the baseline, were normalized with respect to the maximum value of each case; that is, $\Delta R/R_{max}$. The baselines were obtained by waiting for 30 min after turning on the UV-LED to stabilize the sensors. The time interval between gas on and off was set to be 3 min. When the sensors are exposed to the NO_2 gas, the resistances increase as electron depletion layers become wider. In addition, the increments in the resistances are proportional to the concentration of the NO_2 gas. Especially, Sensor C has saturated values of the resistance. As shown in Figure 6a, for 5 ppm, 10 ppm, and 15 ppm NO_2 gas exposures, the saturated values in the *y*-axis of Sensor C are obtained as 25%, 70%, and 100%, respectively. For 10 ppm and 15 ppm of the NO_2 gas, it is observed that there are overshoot characteristics, and the overshoot becomes sharper as the concentration of the NO_2 gas increases. Although the overshoots occur, the response becomes steady and saturated eventually. Moreover, the sensor makes a complete recovery within 3 min after turning off the NO_2 gas. However, Sensor A shows a slow response so that the resistance value does not saturate. Besides, in this case, because the recovery time drags, the sensor fails to make a full recovery. For Sensor B, the rates of the response and recovery are noticeably improved compared to the sensor without annealing. Nevertheless, it is evident that further improvements are still required. Figure 6b enlarges the sensing performance of Sensor C when the sensor was exposed to 15 ppm of the NO_2 gas as a representative. Although there was an overshoot when resistance was increasing, the saturation property was confirmed. The response time, the time to arrive at 90% of the saturated value, is obtained as 82 s. When turning off the NO_2 gas, the curve makes a complete recovery, and the recovery time—the time to recover 90% from the saturated

value to the baseline—is identified as 71 s. Figure 6c depicts the response time and recovery time of Sensor C according to the concentration of the NO_2 gas. When the sensor is exposed to the 10-ppm NO_2, compared to the 5-ppm NO_2, the recovery time shortens, whereas the response takes a longer time because the saturated value is reached after passing through the overshoot characteristic. In contrast, for the higher concentration of the NO_2 gas, 15 ppm, response time decreases, whereas the recovery time becomes extended.
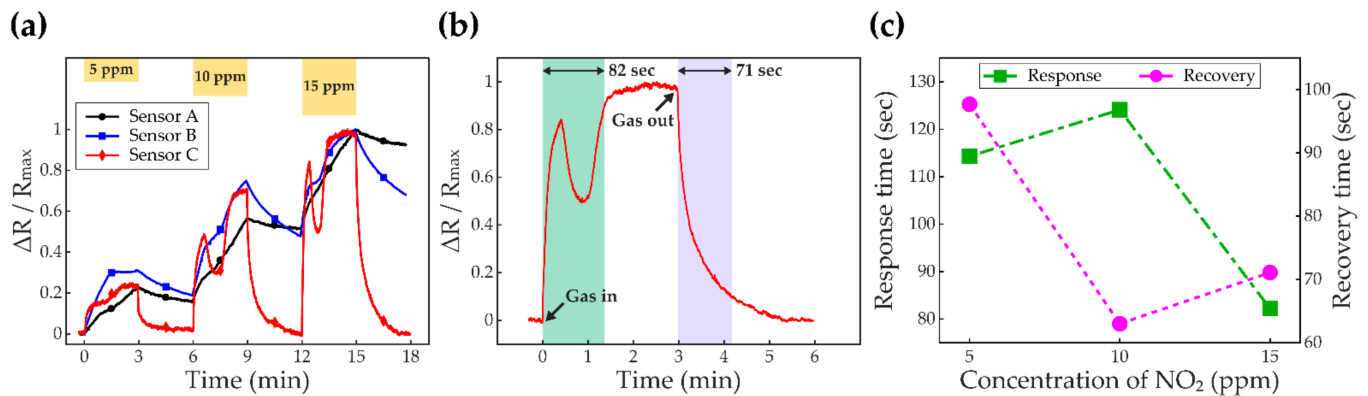
Figure 6. Sensor performances are plotted. (**a**) shows the effects of annealing on performance. The yellow bar graph on the top of (**a**) depicts the concentration of NO_2 with respect to time. The black line marked by the circles shows the response of Sensor A. The blue line labeled by the squares and red line marked by the diamonds plot the responses of Sensor B and Sensor C, respectively. For the y-axis, the resistance increment is normalized with respect to the maximum value of each graph to compare the curve profiles of three sensor types. (**b**) depicts the response of Sensor C when the sensor is exposed to the 15-ppm NO_2 gas. The response time and recovery time are denoted in (**b**) as 82 s and 71 s, respectively. The moments of gas in and out are indicated by the black arrows. (**c**) shows the response time and recovery time of Sensor C. Left and right y-axes indicate the response time and recovery time, respectively. The green square and magenta circle denote the response time and recovery time, respectively.

3.3. Discussion on Sensor Mechanism

Herein, the NO_2 sensing mechanism by TiO_2 NRs and Pt NPs is proposed. Because the contact between TiO_2 and Pt is a metal-semiconductor junction, a Schottky barrier is formed [22]. Illuminating UV photons, the charge separation occurs, possibly due to changes in the surface potential [29]. In this regard, by attaching Pt NPs to TiO_2 NRs, Pt can capture the photogenerated electrons from TiO_2. The electron separated from the electron-hole pair reacts with NO_2 gas at the surface, and subsequently, it leads to intensifying the electron depletion layer of TiO_2, which is the n-type metal oxide semiconductor [39]. It was confirmed that in Figure 6, the resistance of the sensor increases when the sensors are exposed to NO_2 gas.

However, it is known that the photoexcited electrons, traveling in TiO_2, are barely able to reach the surface of TiO_2, which includes the metal-semiconductor junction, when the electron-hole recombination occurs too rapidly [29]. To address this issue, the electron mobility in TiO_2 needs to be fast enough for electrons to pass over from TiO_2 to Pt. As demonstrated in Figure 5, annealing TiO_2 NRs in the fabrication process can significantly improve the crystallinity of the TiO_2 NRs [38]. These annealing processes were conducted at 700 °C in ambient air for 1 h and 2 h after hydrothermally synthesizing TiO_2 NRs as depicted in Figure 1. The improvements in crystallinity quicken the movements of the photogenerated electrons.

Figure 7 illustrates the proposed mechanism described above. Figure 7a is a schematic of Sensor A. As shown in Figure 6a, this type of sensor had poor performance for the too slow response. It is believed that too many electrons are recombined with the holes, and these electrons cannot be involved in the surface reactions. In contrast, Figure 7b,c depict Sensor B and Sensor C, which have the annealed TiO_2 NRs with the improved crystalline characteristics. However, for Sensor B, further improvements in the crystallinity

are still required. Further enhancement can be achieved by annealing TiO$_2$ NRs for 2 h. As demonstrated in Figure 5, Sensor C had better crystallinity than Sensor B. Therefore, the photogenerated electrons run swiftly to reach the interface between TiO$_2$ and Pt before recombinations of the electron-hole pairs. The Pt NPs hold the electrons like electron traps by utilizing the Schottky barriers [21,40]. Finally, it leads to the fast sensing response, as demonstrated in Figure 6, by letting the electrons react with the NO$_2$ gas at the surface.
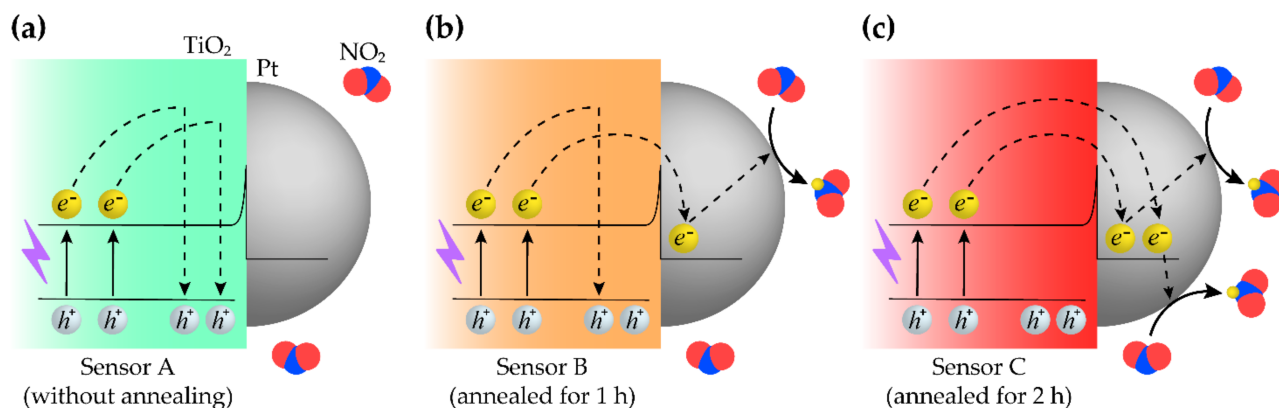
Figure 7. Proposed sensing mechanisms are depicted. Photoelectrochemical activities for sensing NO$_2$ with respect to time of annealing TiO$_2$ are shown. (**a**) is the schematic of Sensor A which did not have an annealing process to TiO$_2$. (**b**) and (**c**) suggest the working mechanisms of Sensor B and Sensor C of which TiO$_2$ NRs were annealed for 1 h and 2 h, respectively. e$^-$ and h$^+$ indicate electron and hole, respectively.

Because for TiO$_2$-Pt, higher crystallinity might yield higher photocatalytic activity at room temperature [41,42], there is a possibility that improvement in crystallinity could lead to enhanced photocatalytic activity. Presumably, there is another chance that wider bandgap with higher crystallinity could strengthen the effects of the Schottky barrier, thereby enhancing the charge separation [43].

As indicated in Figure 3c, for Pt NPs and non-annealed TiO$_2$ NRs, it was noticeable that Pt NPs clumped together to form a chunk of Pt on several locations. Because Pt on these sites might capture holes as well as electrons, the electrons eventually come to recombine with the holes [40]. Consequently, it could contribute to the poor sensing performance of Sensor A. Meanwhile, the UV light illumination induces plasmonic effects in the fine Pt NPs. Because the plasmonic effects can inhibit electron-hole pair recombinations, photoelectrochemical activities are probably enhanced [22]. This improvement is likely to contribute to the faster response of the sensor.

It needs to be noted that a reproducibility study, which is especially important for on-field applications [44], is further required to ensure robust sensor performance. Because humidity probably affects the electron mechanism [34,40], humidity control should be covered in the reproducibility study.

4. Conclusions

In this paper, TiO$_2$ NRs and Pt NPs under UV light irradiation have been proposed for the RT gas sensor. TiO$_2$ NRs were prepared by the hydrothermal synthesis, and the as-prepared TiO$_2$ NRs were annealed in ambient air. It was demonstrated that by analyzing the XRD patterns, the 2-h-annealed TiO$_2$ NRs had significantly improved crystallinity compared to the non-annealed TiO$_2$ NRs. It can lead to the faster movements of the photoactivated electrons and suppressing electron-hole recombinations. Pt NPs were fabricated by sputtering Pt and subsequently, performing RTA in N$_2$ ambiance. FE-SEM images showed that the agglomeration of Pt occurred, and TiO$_2$ NRs were successfully decorated with Pt NPs. By utilizing the Schottky barrier between the Pt-TiO$_2$ junction, the photogenerated electrons can be captured by Pt and exposed to NO$_2$ gas. The plasmonic effects by the fine Pt NPs are believed to further accelerate the separation between the

electron-hole pairs. To evaluate NO_2 gas sensing performance, the experimental platform was set up. In the experiments, the values of resistance of the gas sensor were measured in real-time. It was confirmed that the sensing performance of the sensor with the 2-h-annealed TiO_2 NRs was greatly superior to the performance of the sensor with the 1-h-annealed or non-annealed TiO_2 NRs. It suggests that improving the crystallinity by carrying out thermal treatment is a highly effective method for the photoactivated electrons to reach the surface. Therefore, the 2-h-annealed TiO_2 NRs decorated with the plasmonic Pt NPs have been employed for RT detection of NO_2 gas successfully by using UV photonic energy.

References

1. Guth, D.J.; Mavis, R.D. Biochemical assessment of acute nitrogen dioxide toxicity in rat lung. *Toxicol. Appl. Pharmacol.* **1985**, *81*, 128–138. [CrossRef]
2. Blair, W.H.; Henry, M.C.; Ehrlich, R. Chronic toxicity of nitrogen dioxide: II. Effect on histopathology of lung tissue. *Arch. Environ. Health* **1969**, *18*, 186–192. [CrossRef] [PubMed]
3. Afzal, A.; Cioffi, N.; Sabbatini, L.; Torsi, L. NO_x sensors based on semiconducting metal oxide nanostructures: Progress and perspectives. *Sens. Actuators B* **2012**, *171*, 25–42. [CrossRef]
4. Walker, J.M.; Akbar, S.A.; Morris, P.A. Synergistic effects in gas sensing semiconducting oxide nano-heterostructures: A review. *Sens. Actuators B* **2019**, *286*, 624–640. [CrossRef]
5. Deng, Y. Semiconducting metal oxides: Morphology and sensing performance. In *Semiconducting Metal Oxides for Gas Sensing*; Springer: Singapore, 2019; pp. 53–75.
6. Kato, N.; Kurachi, H.; Hamada, Y. Thick film ZrO_2 NO_x sensor for the measurement of low NO_x concentration. *SAE Trans.* **1998**, *980170*, 312–320.
7. Penza, M.; Vasanelli, L. SAW NO_x gas sensor using WO_3 thin-film sensitive coating. *Sens. Actuators B* **1997**, *41*, 31–36. [CrossRef]
8. Zhuiykov, S.; Nakano, T.; Kunimoto, A.; Yamazoe, N.; Miura, N. Potentiometric NO_x sensor based on stabilized zirconia and $NiCr_2O_4$ sensing electrode operating at high temperatures. *Electrochem. Commun.* **2001**, *3*, 97–101. [CrossRef]
9. Sumizawa, H.; Yamada, H.; Tonokura, K. Real-time monitoring of nitric oxide in diesel exhaust gas by mid-infrared cavity ring-down spectroscopy. *Appl. Phys. B* **2010**, *100*, 925–931. [CrossRef]
10. Spagnolo, V.; Kosterev, A.; Dong, L.; Lewicki, R.; Tittel, F. NO trace gas sensor based on quartz-enhanced photoacoustic spectroscopy and external cavity quantum cascade laser. *Appl. Phys. B* **2010**, *100*, 125–130. [CrossRef]
11. Kumar, R.; Liu, X.; Zhang, J.; Kumar, M. Room-temperature gas sensors under photoactivation: From metal oxides to 2D materials. *Nano Micro Lett.* **2020**, *12*, 1–37. [CrossRef]
12. Choi, H.-J.; Kwon, S.-H.; Lee, W.-S.; Im, K.-G.; Kim, T.-H.; Noh, B.-R.; Park, S.; Oh, S.; Kim, K.-K. Ultraviolet photoactivated room temperature NO_2 gas sensor of ZnO hemitubes and nanotubes covered with TiO_2 nanoparticles. *Nanomaterials* **2020**, *10*, 462. [CrossRef]
13. Tian, X.; Yang, X.; Yang, F.; Qi, T. A visible-light activated gas sensor based on perylenediimide-sensitized SnO_2 for NO_2 detection at room temperature. *Colloids Surf. A* **2019**, *578*, 123621. [CrossRef]
14. Gu, D.; Wang, X.; Liu, W.; Li, X.; Lin, S.; Wang, J.; Rumyantseva, M.N.; Gaskov, A.M.; Akbar, S.A. Visible-light activated room temperature NO_2 sensing of SnS_2 nanosheets based chemiresistive sensors. *Sens. Actuators B* **2020**, *305*, 127455. [CrossRef]
15. Kumar, R.; Goel, N.; Kumar, M. UV-activated MoS_2 based fast and reversible NO_2 sensor at room temperature. *ACS Sens.* **2017**, *2*, 1744–1752. [CrossRef] [PubMed]

16. Liu, B.; Luo, Y.; Li, K.; Wang, H.; Gao, L.; Duan, G. Room-temperature NO_2 gas sensing with ultra-sensitivity activated by ultraviolet light based on SnO_2 monolayer array film. *Adv. Mater. Interfaces* **2019**, *6*, 1900376. [CrossRef]

17. Peng, L.; Zhao, Q.; Wang, D.; Zhai, J.; Wang, P.; Pang, S.; Xie, T. Ultraviolet-assisted gas sensing: A potential formaldehyde detection approach at room temperature based on zinc oxide nanorods. *Sens. Actuators B* **2009**, *136*, 80–85. [CrossRef]

18. Li, X.; Li, X.; Wang, J.; Lin, S. Highly sensitive and selective room-temperature formaldehyde sensors using hollow TiO_2 microspheres. *Sens. Actuators B* **2015**, *219*, 158–163. [CrossRef]

19. Shen, Y.; Zhong, X.; Zhang, J.; Li, T.; Zhao, S.; Cui, B.; Wei, D.; Zhang, Y.; Wei, K. In-situ growth of mesoporous In_2O_3 nanorod arrays on a porous ceramic substrate for ppb-level NO_2 detection at room temperature. *Appl. Surf. Sci.* **2019**, *498*, 143873. [CrossRef]

20. Yan, W.; Hu, M.; Zeng, P.; Ma, S.; Li, M. Room temperature NO_2-sensing properties of WO_3 nanoparticles/porous silicon. *Appl. Surf. Sci.* **2014**, *292*, 551–555. [CrossRef]

21. An, B.-L.; Fu, Y.-H.; Dai, F.-Z.; Xu, J.-Q. Platinum nanoparticle modified TiO_2 nanorods with enhanced catalytic performances. *J. Alloys Compd.* **2015**, *622*, 426–431. [CrossRef]

22. Wang, Q.; Dong, P.; Huang, Z.; Zhang, X. Synthesis of Ag or Pt nanoparticle-deposited TiO_2 nanorods for the highly efficient photoreduction of CO_2 to CH_4. *Chem. Phys. Lett.* **2015**, *639*, 11–16. [CrossRef]

23. Xing, M.-Y.; Yang, B.-X.; Yu, H.; Tian, B.-Z.; Bagwasi, S.; Zhang, J.-L.; Gong, X.-Q. Enhanced photocatalysis by Au nanoparticle loading on TiO_2 single-crystal (001) and (110) facets. *J. Phys. Chem. Lett.* **2013**, *4*, 3910–3917. [CrossRef]

24. Fu, C.; Li, M.; Li, H.; Li, C.; guo Wu, X.; Yang, B. Fabrication of Au nanoparticle/TiO_2 hybrid films for photoelectrocatalytic degradation of methyl orange. *J. Alloys Compd.* **2017**, *692*, 727–733. [CrossRef]

25. Dhawale, D.S.; Gujar, T.P.; Lokhande, C.D. TiO_2 nanorods decorated with Pd nanoparticles for enhanced liquefied petroleum gas sensing performance. *Anal. Chem.* **2017**, *89*, 8531–8537. [CrossRef]

26. Xiang, C.; She, Z.; Zou, Y.; Cheng, J.; Chu, H.; Qiu, S.; Zhang, H.; Sun, L.; Xu, F. A room-temperature hydrogen sensor based on Pd nanoparticles doped TiO_2 nanotubes. *Ceram. Int.* **2014**, *40*, 16343–16348. [CrossRef]

27. Subha, P.; Hasna, K.; Jayaraj, M. Surface modification of TiO_2 nanorod arrays by Ag nanoparticles and its enhanced room temperature ethanol sensing properties. *Mater. Res. Express* **2017**, *4*, 105037. [CrossRef]

28. Guo, L.; Yin, H.; Xu, M.; Zheng, Z.; Fang, X.; Chong, R.; Zhou, Y.; Xu, L.; Xu, Q.; Li, J. In situ generated plasmonic silver nanoparticle-sensitized amorphous titanium dioxide for ultrasensitive photoelectrochemical sensing of formaldehyde. *ACS Sens.* **2019**, *4*, 2724–2729. [CrossRef] [PubMed]

29. Yoo, H.; Bae, C.; Yang, Y.; Lee, S.; Kim, M.; Kim, H.; Kim, Y.; Shin, H. Spatial charge separation in asymmetric structure of Au nanoparticle on TiO_2 nanotube by light-induced surface potential imaging. *Nano Lett.* **2014**, *14*, 4413–4417. [CrossRef]

30. Hashimoto, K.; Irie, H.; Fujishima, A. TiO_2 photocatalysis: A historical overview and future prospects. *Jpn. J. Appl. Phys.* **2005**, *44*, 8269. [CrossRef]

31. Liu, B.; Aydil, E.S. Growth of oriented single-crystalline rutile TiO_2 nanorods on transparent conducting substrates for dye-sensitized solar cells. *J. Am. Chem. Soc.* **2009**, *131*, 3985–3990. [CrossRef]

32. Mansoor, M.A.; Yusof, F.B.; Nay-Ming, H. Optimization of conditions for improved solar energy harvesting application by hydrothermally grown TiO_2 nanorods. *J. Iran. Chem. Soc.* **2019**, *16*, 1113–1122. [CrossRef]

33. Sun, Y.; Yan, K.; Wang, G.; Guo, W.; Ma, T. Effect of annealing temperature on the hydrogen production of TiO_2 nanotube arrays in a two-compartment photoelectrochemical cell. *J. Phys. Chem. C* **2011**, *115*, 12844–12849. [CrossRef]

34. Zhao, G.; Xuan, J.; Gong, Q.; Wang, L.; Ren, J.; Sun, M.; Jia, F.; Yin, G.; Liu, B. In situ growing double-layer TiO_2 nanorod arrays on new-type FTO electrodes for low-concentration NH_3 detection at room temperature. *ACS Appl. Mater. Interfaces* **2020**, *12*, 8573–8582. [CrossRef]

35. Prathan, A.; Sanglao, J.; Wang, T.; Bhoomanee, C.; Ruankham, P.; Gardchareon, A.; Wongratanaphisan, D. Controlled structure and growth mechanism behind hydrothermal growth of TiO_2 nanorods. *Sci. Rep.* **2020**, *10*, 1–11. [CrossRef] [PubMed]

36. Yang, Z.; Wang, B.; Cui, H.; An, H.; Pan, Y.; Zhai, J. Synthesis of crystal-controlled TiO_2 nanorods by a hydrothermal method: Rutile and brookite as highly active photocatalysts. *J. Phys. Chem. C* **2015**, *119*, 16905–16912. [CrossRef]

37. Ismail, A.A.; Al-Sayari, S.A.; Bahnemann, D. Photodeposition of precious metals onto mesoporous TiO_2 nanocrystals with enhanced their photocatalytic activity for methanol oxidation. *Catal. Today* **2013**, *209*, 2–7. [CrossRef]

38. Wang, X.; Zhang, D.; Xiang, Q.; Zhong, Z.; Liao, Y. Review of water-assisted crystallization for TiO_2 nanotubes. *Nanomicro Lett.* **2018**, *10*, 1–28. [CrossRef]

39. Kim, H.-J.; Lee, J.-H. Highly sensitive and selective gas sensors using p-type oxide semiconductors: Overview. *Sens. Actuators B* **2014**, *192*, 607–627. [CrossRef]

40. Wang, W.-N.; An, W.-J.; Ramalingam, B.; Mukherjee, S.; Niedzwiedzki, D.M.; Gangopadhyay, S.; Biswas, P. Size and structure matter: Enhanced CO_2 photoreduction efficiency by size-resolved ultrafine Pt nanoparticles on TiO_2 single crystals. *J. Am. Chem. Soc.* **2012**, *134*, 11276–11281. [CrossRef] [PubMed]

41. Devi, L.G.; Kavitha, R. A review on plasmonic metal TiO2 composite for generation, trapping, storing and dynamic vectorial transfer of photogenerated electrons across the Schottky junction in a photocatalytic system. *Appl. Surf. Sci.* **2016**, *360*, 601–622. [CrossRef]

42. Qi, L.; Ho, W.; Wang, J.; Zhang, P.; Yu, J. Enhanced catalytic activity of hierarchically macro-/mesoporous Pt/TiO_2 toward room-temperature decomposition of formaldehyde. *Catal. Sci. Technol.* **2015**, *5*, 2366–2377. [CrossRef]

43. Saravanan, R.; Aviles, J.; Gracia, F.; Mosquera, E.; Gupta, V.K. Crystallinity and lowering band gap induced visible light photocatalytic activity of TiO$_2$/CS (Chitosan) nanocomposites. *Int. J. Biol. Macromol.* **2018**, *109*, 1239–1245. [CrossRef] [PubMed]
44. Gaiardo, A.; Zonta, G.; Gherardi, S.; Malagù, C.; Fabbri, B.; Valt, M.; Vanzetti, L.; Landini, N.; Casotti, D.; Cruciani, G. Nanostructured SmFeO$_3$ gas sensors: Investigation of the gas sensing performance reproducibility for colorectal cancer screening. *Sensors* **2020**, *20*, 5910. [CrossRef] [PubMed]